J. Astrophys. Astr. (2010) **31,** 59–79

Determination of the Mean HI Absorption of the Intergalactic Medium

A. Aghaee[1,2,*], P. Petitjean[3], R. Srianand[4], C. S. Stalin[5] & R. Guimarães[6]
[1]*Department of Physics, University of Sistan and Baluchestan, Zahedan 98135-674, Iran.*
[2]*School of Astronomy, Institute for Research in Fundamental Sciences (IPM), P. O. Box 19395-5531, Tehran, Iran.*
[3]*Institut d'Astrophysique de Paris, Université Paris 06 & CNRS, UMR7095, 98bis Bd Arago, 75014 Paris, France.*
[4]*Inter-University Centre for Astronomy and Astrophysics, Post Bag 4, Ganeshkhind, Pune 411 007, India.*
[5]*Indian Institute of Astrophysics, Koramangala, Bangalore 560 034, India.*
[6]*Universidade de Feira de Santana, Av. Transnordestinam S/N, 40036-900, Feira de Santana, BA - Brasil.*
[*]*e-mail: aghaee@ipm.ir*

Received 2009 September 14; accepted 2010 April 19

Abstract. In recent years, the Lyman-α forest in quasar spectra has been used, together with N-body simulations, to determine the underlying matter distribution in the intergalactic medium (IGM). One of the key parameters to be known in order to compare observations and numerical simulations is the mean HI absorption in the IGM. To derive the latter, one has first to fit the quasar continuum. We have observed 20 high redshift and highly luminous QSOs ($m_{\rm V} \leq 17.5$ and $2.40 \leq z_{\rm em} \leq 3.91$) at intermediate spectral resolution, with either EMMI (ESO Multi-Mode Instrument) on the ESO-NTT telescope or CARELEC at the OHP (Observatoire de Haute-Provence), and applied different methods of determining the QSO continuum to this QSO sample. We have measured the amount of absorption, known as the flux decrement, *DA*, in the Lyman-α forest for these different methods and compared the results. In addition, we have compared *DA* values measured along the same lines of sight observed at high and intermediate spectral resolutions. We discuss the systematics resulting from the use of automatic continuum fitting methods.

Key words. Quasar: absorption lines—galaxies: intergalactic medium.

1. Introduction

The numerous absorption lines seen in the spectra of distant quasars (QSO) bluewards of the Lyman-α emission line from the quasar, the so-called Lyα forest, reveal the intergalactic medium (IGM) up to redshift larger than 6. The Lyα forest was predicted and first detected by Gunn & Peterson (1965). It provides information on the overall matter distribution on scales smaller than those accessible with other observables as the Cosmic Microwave Background (CMB) (e.g., Croft *et al.* 1998; Pichon *et al.*

2001; McDonald *et al.* 2005). Our physical understanding of the IGM, comes from the detailed comparison between the results of N-body numerical simulations of the growth of structures in the universe and observations of the Lyman-α absorption lines (e.g., Petitjean 1999; Theuns 2005). However, to do so, simulations must be normalized because they are not able to predict the mean absorption in the IGM that depends on the UV flux produced by quasars and galaxies. The total amount of absorption by neutral hydrogen has to be derived from observations (e.g., Rauch *et al.* 1997; Rauch 1998).

In order to measure this absorption, the intrinsic QSO continuum has to be determined over the Lyman-α forest. In spite of the many measurements published in the literature (e.g., Schneider *et al.* 1991; Press *et al.* 1993; Rauch *et al.* 1997; Becker *et al.* 2001; Kim *et al.* 2001, 2007; Bernardi *et al.* 2003; Seljak *et al.* 2003; White *et al.* 2003; Aracil *et al.* 2004; Songaila 2004; Tytler *et al.* 2004; Kirkman *et al.* 2005, 2007; Faucher-Giguère *et al.* 2008; Dall'Aglio *et al.* 2009) no concensus has been reached yet on what is the best method to determine the continuum. It is well known that the continuum derived by independent groups for the same quasar can differ by more than 20% over a non-negligible fraction of the spectrum (see e.g., Nusser & Haehnelt 2000 comparing data from Rauch *et al.* 1997 and Songaila & Cowie 1996). Because of this, although the broad picture describing the IGM might be correct, the measurement of the power spectrum is limited by uncertainties in the determination of the QSO continuum for scales larger than $\sim 12\,\mathrm{h}^{-1}$ Mpc (Croft *et al.* 1999).

Here we would like to critically apply different methods to derive the continuum of quasar spectra in the Lyman-α forest and to discuss their influence on the determination of the mean HI absorption of the IGM and its evolution with redshift. We present the observations in section 2, describe data reduction in section 3, apply different methods to determine the continuum of quasars in our sample in section 4, derive the mean HI absorption in the IGM in section 5, compare the measurements performed from intermediate and high-resolution data in section 6 and conclude in section 7.

2. Observations

We have observed at low and intermediate spectral resolution a sample of 20 bright and high redshift quasars with either the ESO Multi-Mode Instrument (EMMI) on the New Technology Telescope (NTT) of the European Southern Observatory (ESO) or the CARELEC spectrograph on the 1.93 m telescope of the Observatoire de Haute Provence (OHP). Details are given in Table 1.

Eight quasars with $m_{\mathrm{V}} \leq 17.5$ and $2.40 \leq z_{\mathrm{em}} \leq 3.78$ have been observed with EMMI in July 2004 (Aghaee *et al.* 2005). This instrument is divided in two arms covering wavelength ranges from 3000 to 5000 Å in the blue arm and from 4000 to 10,000 Å in the red arm. For the highest redshift quasars, we used the red arm with grating R#7, binning 2×2, in two of the ranges 4750–6300 Å or 5200–6700 Å, and 5900–7400 Å or 6450–7850 Å. For the lowest redshift quasar, we used the blue arm with grating B#12, binning 1×1, in the ranges 3400–4300 Å and 4200–5100 Å. For intermediate redshift quasars, we used both arms with grating R#7 in the red and B#12 in the blue. Both gratings have 600 lines/mm. At 6000 Å, grating R#7 has an efficiency of 68% and leads to a dispersion of 0.82 Å/pix resulting in a spectral resolution of $R \sim 2600$ with a $1''$ slit and 2×2 binning. The efficiency of the grating B#12, at

Table 1. Sample and observational details.

No.	Name	z_{em}	Telescope	T.E.T[(1)] (s)	SNR[(2)]	m_V
1	APM 08279 + 5255	3.911	OHP	7200	62	15.2
2	PKS 2000 − 330	3.783	NTT+VLT	9000	40	17.3
3	B 1422 + 231	3.620	OHP	3600	58	16.5
4	PKS 2126 − 158	3.266	NTT+VLT	5400	39	17.0
5	HS 0741 + 4741	3.210	OHP	7200	43	16.2
6	S4 0636 + 68	3.177	OHP	9000	44	16.6
7	SBS 1425 + 606	3.164	OHP	10,800	87	16.6
8	HS 1946 + 7658	3.051	OHP	11,500	70	16.2
9	S5 1759 + 75	3.050	OHP	7200	32	16.5
10	HS 1248 + 7102	2.990	OHP	14,400	38	16.7
11	HE 2347 − 4342	2.885	NTT+VLT	4200	13	16.3
12	Q 1511 − 091	2.878	NTT	3600	20	17.5
13	CSO 1107 (Q 1542 + 311)	2.830	OHP	3600	15	17.1
14	Q 0002 − 422	2.758	NTT+VLT	4000	22	17.2
15	HE 0151 − 4326	2.740	NTT+VLT	5000	31	16.8
16	HS 1700 + 6416	2.736	OHP	7200	54	16.2
17	CSO 1061 (Q 1444 + 2919)	2.669	OHP	7200	40	16.2
18	CSO 38 (Q 1009 + 299)	2.620	OHP	7200	54	16.4
19	HE 1347 − 2457	2.534	NTT+VLT	5400	22	16.8
20	HE 2217 − 2818	2.406	NTT+VLT	5200	24	16.0

[(1)]Total exposure time; [(2)]Signal-to-noise ratio measured at 6500 Å for the OHP, and near the Si IIλ1304 emission line for the NTT.

$\lambda = 3500$ Å is $\sim 65\%$. Dispersion at 4000 Å is 0.92 Å/pix leading to $R \sim 1700$ for 1×1 binning and $1''$ slit.

Twelve luminous and high redshift quasars ($m_V \leq 16.7$ and $2.62 \leq z_{em} \leq 3.91$; see Table 1) have been observed at intermediate spectral resolution with the CARELEC spectrograph at the OHP in March 2006 (Aghaee *et al.* 2006). The grating used is B#12 with 300 lines/mm and blaze wavelength of 5000 Å. Dispersion is 133 Å/mm and leads to a spectral resolution of ~ 900 at 5000 Å for a wavelength range 3600–7000 Å.

3. Data reduction

The purpose of the data reduction is to convert the two-dimensional raw CCD images into a one-dimensional spectrum giving the atmosphere corrected object flux as a function of wavelength. The data reduction was performed using standard procedures available in the long slit context of the reduction system ESO-MIDAS (Munich Image Data Analysis System). A number of CCD pixels are spoiled by the consequences

of cosmic ray impacts. The corresponding artificially high values are removed by median filtering over a 3×3 window, excluding the spoiled central pixel. A master bias, constructed from a large number of individual bias exposures, is subtracted to all frames. Due to several effects, including differential sensitivity of the pixels, residual diffusion of light in the instrument or fringing, a uniformly illuminated CCD will not give a uniform signal in the image frame. This non-uniformity is corrected by dividing each frame by a normalized flat-field generated by median combining a large number of flat-field frames. For the wavelength calibration we use either the He+Ar or ThAr lamp, depending on the resolution and wavelength range of the spectrograph configuration (Gonzalez *et al.* 2006). The spectrum was extracted using the algorithm that delivers the maximum possible signal-to-noise ratio while preserving spectrophotometric accuracy (Horne 1986). Wavelengths were air-vacuum corrected using the Edlén (1966) formula and converted in the heliocentric reference frame. Flux calibration was performed by observing a standard star with the same instrumental configuration and reducing the spectrum in exactly the same way as the object spectrum. Finally, atmospheric extinction correction was performed using the airmass, and the extinction law given for the observatory where the observation was performed.

4. Determination of the QSO continuum

The QSO continuum in the Lyman-α forest is notoriously difficult to determine in general but particularly at high redshift where the Lyman-α forest is so dense that there remains few if any unabsorbed portions of the spectrum. In addition, most spectroscopic data available on QSOs are of intermediate resolution ($R \sim 2000$ for SDSS) and unabsorbed pixels, after convolution by the instrument response, can be affected by nearby Lyman-α absorptions. Here we want to compare the results of applying different continuum fitting methods to the same data to characterize the typical uncertainties related to the choice of the method. For this, we will calculate the amount of absorption from the IGM, characterized by the flux decrement in the Lyman-α forest, *DA*, defined as:

$$DA = \frac{1}{(\lambda_2 - \lambda_1)} \int_{\lambda_1}^{\lambda_2} \frac{(F_{\rm Cont} - F_{\rm Obs})}{F_{\rm Cont}} d\lambda, \quad (1)$$

where $F_{\rm Cont}$ is the flux in the continuum derived from different methods and $F_{\rm Obs}$ is the observed flux.

Table 2 lists the methods we could apply to each of the quasar spectra in our sample. The derived continua are shown for each quasar in the Appendix.

4.1 *The power law (PL) method*

The overall shape of the quasar continuum is often modelled as a power law plus emission lines. One of the standard methods is to extrapolate in the Lyman-α forest the power-law (PL) calculated over wavelengths redward of the Lyman-α emission line. This method is very convenient as the red part of the quasar spectrum is well defined. It assumes, however that:

(i) there is no break of the power law between the red and blue parts of the spectrum,

Table 2. Details of the continuum fitting to the QSO spectra.

No.	Name	$z_{\rm em}$	α_ν	Continuum			
				PL[(1)]	PCS[(2)]	IE[(3)]	SL[(4)]
1	APM 08279 + 5255	3.911	−1.91016	√		√	√
2	PKS 2000 − 330	3.783	−0.78169	√	√	√	√
3	B 1422 + 231	3.620	0.66013	√	√	√	√
4	PKS 2126 − 158	3.266	−1.48501	√		√	√
5	HS 0741 + 4741	3.210	−0.40579	√	√	√	√
6	S4 0636 + 68	3.177	−0.66045	√	√	√	√
7	SBS 1425 + 606	3.164	0.07775	√	√	√	√
8	HS 1946 + 7658	3.051	−0.70512	√	√	√	√
9	S5 1759 + 75	3.050	−0.79154	√	√	√	√
10	HS 1248 + 7102	2.990	−0.42653	√	√	√	√
11	HE 2347 − 4342	2.885				√	√
12	Q 1511 − 091	2.878	−0.77611	√		√	√
13	CSO 1107 (Q 1542 + 311)	2.830	−0.57063	√	√	√	√
14	Q 0002 − 422	2.758	−0.13941	√		√	√
15	HE 0151 − 4326	2.740	−0.77611	√			√
16	HS 1700 + 6416	2.736	−1.00146	√	√	√	√
17	CSO 1061 (Q 1542 + 311)	2.669	−0.49030	√	√	√	√
18	CSO 38 (Q 1009 + 299)	2.620	−0.19294	√	√	√	√
19	HE 1347 − 2457	2.534	−2.01185	√		√	√
20	HE 2217 − 2818	2.406	−1.01641	√		√	√
	Median	2.990	−0.70512				

[(1)]PL: Power-law; [(2)]PCS: Principal component spectra; [(3)]IE: Iterative estimating; [(4)]SL: Smooth local.

(ii) that emission lines located between the QSO Lyman-α and Lyman-β emission lines are not prominent, and
(iii) that the observed wavelength range is large enough to get a good determination of the spectral slope.

The first assumption may not be correct as a few authors have pointed out that the slope of the quasar continuum could change at $\sim$1200 Å (Zheng *et al.* 1997; Binette *et al.* 2003). The second assumption is not correct as there exist emission lines especially near 1073 and 1123 Å (Vanden Berk *et al.* 2001). The corresponding features are often considered within errors.

We fitted a function $f_\lambda = A\lambda^{\alpha_\lambda}$, where $\alpha_\lambda = -2 - \alpha_\nu$, to the spectrum longward of the Lyman-α emission using the available wavelength ranges devoided of emission lines (see Appendix). The resulting values derived for α_ν are given in Table 2.

The median value of the power-law index, α_ν, is ~ -0.7. This value is very similar to what was found by many researchers (e.g., Richston & Schmidt 1980; Sargent

et al. 1989; Pentericci *et al.* 2003). Note however that determinations using optical and infra-red data seem to indicate that the slope is harder for most of the quasars ($\alpha_\nu \sim -0.3$, Francis 1996). The latter author conclude that quasars could have an intrinsic continuum slope of $\alpha \sim 0.3$ but are reddened by various amounts of dust (see also Webster *et al.* 1995).

4.2 *Principal component analysis (PCA) method*

In the past, principal component analysis has been performed to decompose the spectrum of quasars with the aim to classify these objects (Francis *et al.* 1992). More recently, Suzuki *et al.* (2005) used PCA to find correlations between the red ($\lambda > 1200$ Å) and blue ($\lambda < 1200$ Å) parts of the spectra in order to derive the continuum in the Lyman-α forest from the red continuum. These authors have shown that the three first components account for, respectively, 63.4, 14.5, and 6.2% of the variance and the first ten components reproduce 96% of the total variance. The first component carries the Lyman-α, Lyman-β and high ionization emission line features (O VI, N V, Si IV, C IV) that are sharp and strong. The second component carries low ionization emission line features (Fe II, Fe III, Si II, C II) that are broad and weak.

We applied this method to the QSO spectra in our sample which show the C IV emission line (see Appendix). The fully automatic method works pretty well to recover the rest-wavelength range between the Lyman-β+O VI emission-line blend at $\sim$ 1025 Å and the C IV emission line at $\sim$ 1600 Å in the rest frame. In particular it reproduces well the weak emission lines in the Lyman-α forest.

However, important departures from the true continuum is seen in the wings of strong emission lines. In addition, the method happens to be unstable for some spectra and returns obviously wrong continua with no apparent reason (see Appendix).

4.3 *The iterative estimating (IE) method*

In the iterative estimating (IE) method (Aracil *et al.* 2004), the continuum is produced iteratively by minimizing the sum of a regularisation term and a χ^2 term. In our case the regulation matrix is simply the unit matrix. The procedure smooths the continuum on a fixed scale and the χ^2 term is computed from the difference between the quasar spectrum and the continuum estimated during the previous iteration. The effect of the former is to increase the errors when the difference between the spectrum and the continuum is large (e.g., when absorption occurs) so that the weights of the corresponding pixels in the χ^2 minimization is reduced. A smoothing parameter allows to vary the scale of the scheme.

This procedure is very successful in suppressing the strong absorption lines from a local estimate of the continuum and works very well at low redshift. At high redshift, however, the method underestimates the overall absorption in the Lyman-α forest. The reason is that it assumes, by construction, that most of the points outside strong absorption features are representative of the intrinsic QSO continuum. This is a crude assumption because (i) blending of intervening Lyman-α absorptions is strong for $z > 3$ and (ii) a somewhat low spectral resolution convolves the spectrum on scales larger than the width of a typical absorption feature. The procedure of continuum fitting smooths the quasar continuum over some scale. We have tested two

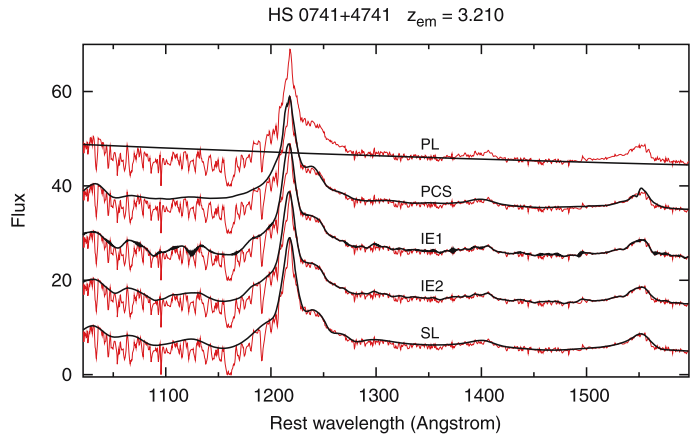

Figure 1. The continua of QSO HS 0741+4741 derived from applying the different methods described in the text to the same spectrum. Each spectrum has been shifted upward by 10 on an arbitrary flux scale with respect to the bottom spectrum.

smoothing scales corresponding to IE1 and IE2. The IE1 and IE2 continua are, respectively, the lowest and highest reasonable continua obtained after varying the smoothing parameter.

4.4 *The smooth local (SL) method*

The smooth local (SL) method fits the continuum of a spectrum to regions of the Lyman-α forest deemed 'free of absorption lines' *as judged by eye*. This is done by identifying unabsorbed regions within the forest and by connecting them with smoothing splines.

As for the IE method, one of the advantages of this method is that it does not need to make any assumption on the red part of the spectrum. The important disadvantage is that it is observer dependent. However, as will be seen in the following, a trained observer is a very efficient and successful neurone network (see section 6).

4.5 *Discussion*

As an example, we show in Fig. 1 the spectrum of QSO HS 0741+4741 together with the continua obtained when using the different methods described above. All the other QSO spectra and their different continuum estimates are shown in the Appendix.

As can be seen in the figure, the result of the PL method seems very high. This is apparent at the position of the Lyman-β emission line. Although a few quasar spectra can be affected by inadequate flux correction in the very blue, this is probably not the case for this quasar. This therefore shows the limit of this method: it is not suited when the slope in the red wavelength range is not representative to that in the blue or if the wavelength range in the red of the spectrum is not adequate to derive the red-side index. The PCA continuum as well looks slightly high especially around 1125 Å. This is probably a consequence of the vicinity of the emission line that has a hump at $\sim$ 1175 Å. The reader may have thus a feeling of the unstable nature of this method.

Indeed it works pretty well for a non-negligible number of quasars but it can also lead to unpredictable large departures from any reasonable continuum.

On the contrary, the IE method using the lowest smoothing scale, IE1, appears low in some wavelength ranges (especially around 1090 Å). This is related to the fact that this method has problems to make the continuum jump over adjacent absorptions. The other two continua, obtained from the IE2 and SL methods, give approximately the same results that look good to an expert eye.

In the following, we will compare the mean absorption in the Lyman-α forest measured using the different continuum fitting methods.

5. Flux decrement determination

We restrict our analysis to the wavelength range from $\lambda_{\mathrm{Ly}\beta}(1 + 3000(\mathrm{km/s})/c)$ to $\lambda_{\mathrm{Ly}\alpha}(1 - 5000(\mathrm{km/s})/c)$, where c is the speed of light, to avoid the proximity effect close to the QSO and to avoid confusion owing to an overlap of intervening Lyman-α and associated Lyman-β absorptions. We averaged DA over intervals of redshift path $\Delta z = 0.1$. We identified and masked the strong DLA lines. Note that the metal lines were not masked in our analysis because of insufficient resolution of our data. We discarded redshift intervals where $>50\%$ of the pixels were removed by this masking procedure.

In the upper panel of Fig. 2, we plot *versus* redshift all the measurements performed in our sample for the five estimated continua. The large dispersion in the points at a given redshift is due to the cosmic variance in the IGM. It is present even for the low redshift QSOs (e.g., Kirkman *et al.* 2007).

For each method we have fitted a power law $DA(z) = A(1 + z)^{\alpha}$ to the measurements. Best values for A and α are given in Table 3 and the power laws are overplotted on top of the individual measurements in Fig. 2. Last row of Table 3 gives the parameter values derived when all measurements are taken into account. This could be a way to smooth the differences between different methods. As can be seen in Fig. 2 and as expected, the different methods give similar results at $z \sim 2$ and differ more and more as redshift increases. It can be seen that the PL and PCA methods give values of *DA* higher than the IE method for any smoothing parameter. The non-automatic SL method gives measurements intermediate between the automatic methods. This is our preferred method.

In the bottom panel of Fig. 2, we average the *DA* measurements along all lines of sight in bins of $\Delta z = 0.2$ and this for the different methods. The number of lines of sight per bin is at least 3 and up to 10. Errors are taken as the standard deviation of the points in the bin divided by the square root of the number of points. Our results are compared with the result of Songaila (2004), Kirkman *et al.* (2005), Kim *et al.* (2007), Faucher-Guiguére *et al.* (2008) and the recent results of Dall'Aglio *et al.* (2009) which is derived from a sample of 1733 SDSS QSOs.

6. DA from high and intermediate spectral resolution spectra

Seven quasars in our sample have been observed with both UVES, at high resolution, and EMMI at intermediate resolution (see Table 1). In Fig. 3, we show an example of a QSO observed at intermediate resolution ($R \simeq 2300$) with EMMI at the NTT and at high spectral resolution ($R \simeq 45{,}000$) and high S/N ratio (~ 100 at 6000 Å) with UVES at the VLT. The ratio of the continua derived from the intermediate and the high

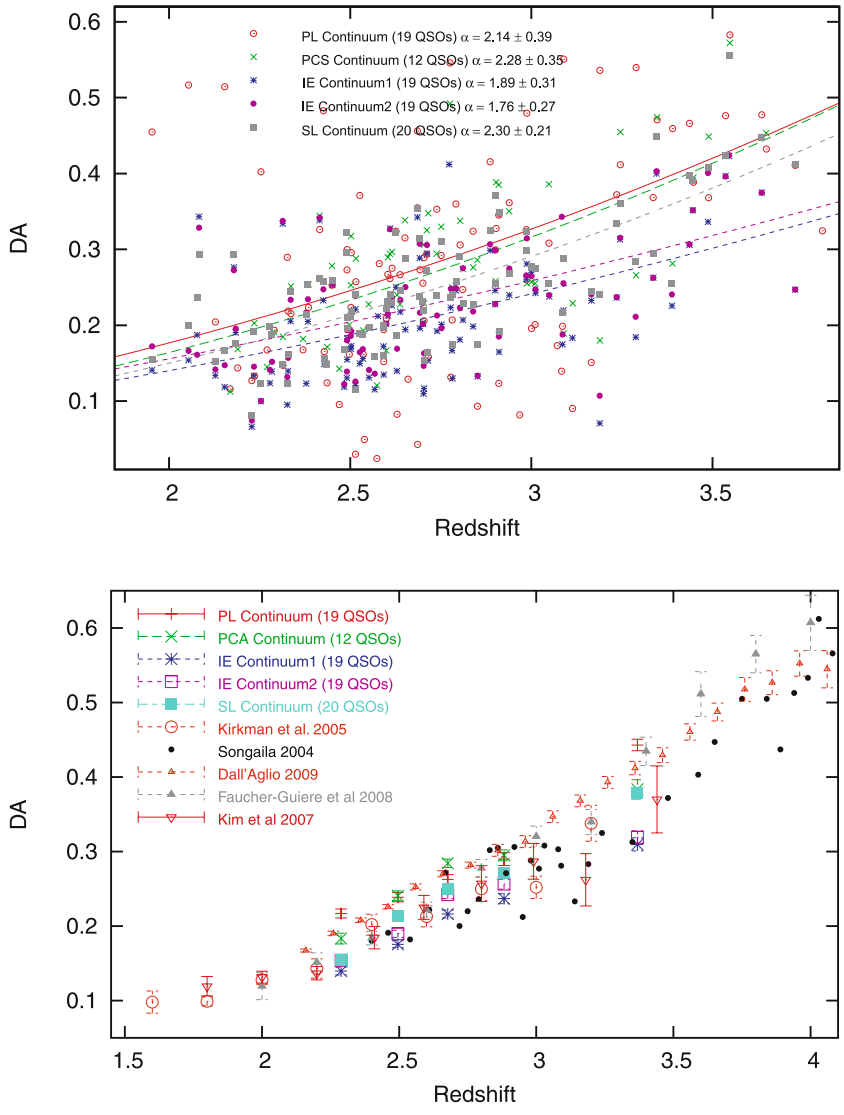

Figure 2. *DA versus* redshift for the OHP-CARELEC and NTT-EMMI data and different continuum fitting methods. Strong Lyman-α absorption lines have been masked (see text). *Top panel:* Each point shows the mean absorption in the IGM, *DA*, in bins of $\Delta z = 0.1$ for each QSO and each method. The curves are the best fit power-laws, $DA(z) = A(1+z)^{\alpha}$, for the different continuum fitting methods: from the top, first curve: PL (solid line), second curve: PCA (long dashed line), third curve: SL (short dashed line), fourth curve: IE2 (dotted line), and fifth curve: IE1 (thick short dashed line). *Bottom panel:* Each point corresponds to the mean *DA* in bins of $\Delta z = 0.2$ calculated using all QSOs with 3 to 10 lines of sight per bin. Previous measurements by Songaila (2004), Kirkman *et al.* (2005), Kim *et al.* (2007), Faucher-Guiguére *et al.* (2008) and Dall'Aglio *et al.* (2009) are overplotted.

resolution observations is also shown in the figure. The QSO continua derived from intermediate and high spectral resolution data have been obtained using the SL and IE methods, respectively. As can be seen in this figure, the IE method works very well, at

Table 3. Parameters of the $DA(z)$ power-laws fitted to the DA measurements (see Fig. 2).

Method	A	σ_A	α	σ_α
PL	0.0169199	0.008962	2.1357	0.3865
PCA	0.0134309	0.006470	2.2786	0.3523
IE1	0.0176294	0.007438	1.8877	0.3111
IE2	0.0225284	0.008143	1.7606	0.2669
SL	0.0120169	0.003512	2.2980	0.2142
All	0.0157060	0.003249	2.0882	0.1517

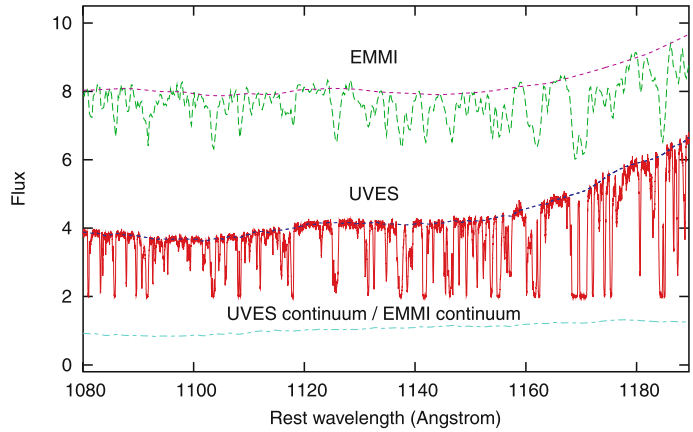

Figure 3. HE 2347−4342 has been observed at intermediate resolution ($R \simeq 2300$) with EMMI at the NTT (top spectrum) and at high spectral resolution ($R \simeq 45{,}000$) and high S/N ratio ($\sim$100 at 6000 Å) with UVES at the VLT (middle spectrum). The upper smooth curves are the continua. The ratio of the continua is shown in the bottom panel.

least at redshift $z \leq 3.5$, for high spectral resolution spectra (see Aracil *et al.* 2004). The reason is simply that the resolution is high enough and the redshift low enough so that adjacent absorptions are not strongly blended. The mean DA values calculated over the wavelength range of Fig. 3, more than 100 Å, is 0.230 and 0.233 at high and intermediate resolutions, respectively. The spectral resolution ratio is about 20 but the difference between the two DA values is just about 1.5%. This may indicate that the systematic corrections applied by Dall'Agglio *et al.* (2009) could be overestimated and in any case questionable. These corrections were introduced because it was believed that the DA measurements from low-resolution data are biased towards lower DA compared to high-resolution data because of the additional blending of absorption lines introduced by the resolution convolution.

In Fig. 4, we compare DA values measured along the same lines of sight observed at both high and intermediate spectral resolution and this for different methods. Wavelength bins are of 200 Å and six or seven QSOs, depending on the applied method (see Table 2), are used. It can be seen from Fig. 4, that the results of fitting intermediate resolution data with the IE1 method are systematically low. They are relatively good for the IE2 method at low DA (or, equivalently, at low redshift, $z < 3.5$). The SL

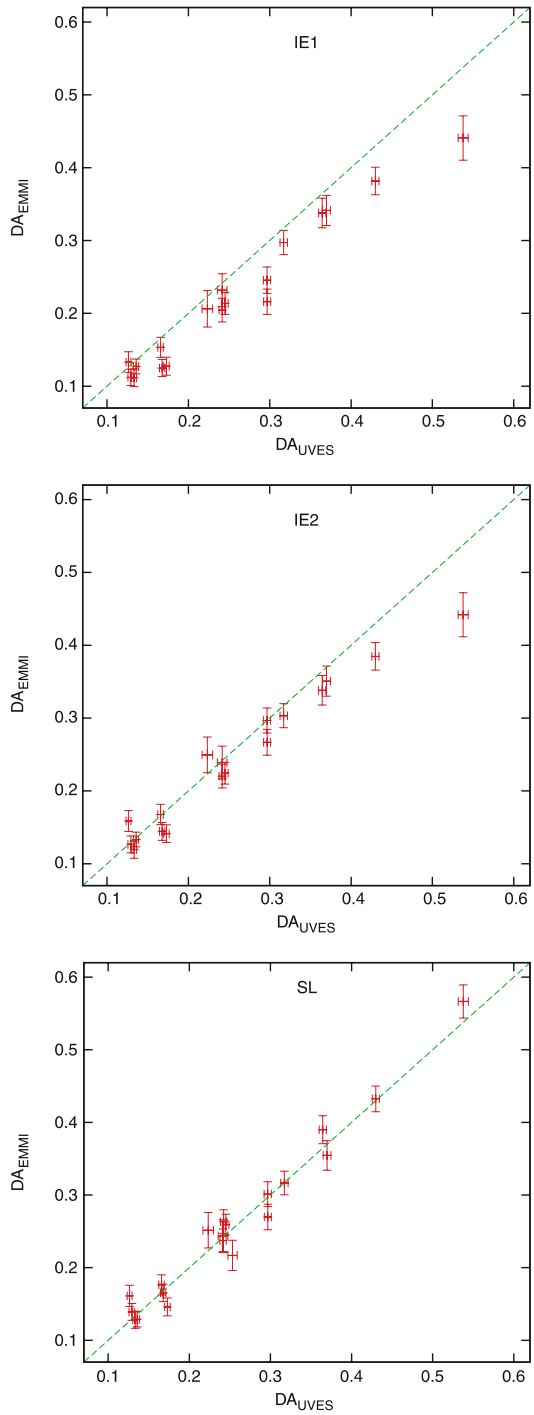

Figure 4. *DA* measured from EMMI spectra and for different methods *versus DA* measured from UVES spectra of the same objects. Seven QSOs are used and each point corresponds to a wavelength range of $\Delta\lambda = 200$ Å. We did not mask any line. The solid diagonal line is drawn to help visual comparison.

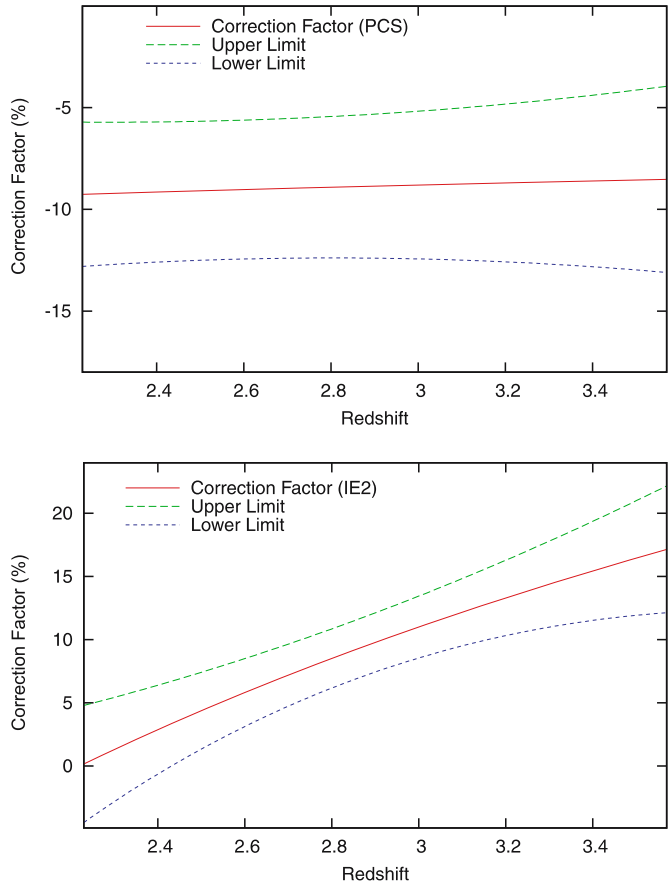

Figure 5. Correction factors to apply to the *DA* value estimated from an automatic procedure: the PCA method (*top panel*) or IE2 method (*bottom panel*) for data at intermediate spectral resolution. The green and blue dotted lines show the upper and lower limits of the correction factor, respectively.

method gives the best results. Unfortunately, the observed NTT wavelength ranges for six out of seven QSOs which have been observed with UVES, are not convenient to apply the PCA and PL methods.

6.1 *Correction factors*

According to the results of the previous section, the SL method gives the best estimate of the quasar continuum. Since it is not an automatic procedure, we can imagine to use an automatic procedure and to correct the resulting *DA* measurements from a systematic deviation between the automatic procedure and the SL procedure. The correction factors defined as:

$$CF_{\mathrm{PCA}}(z) = \frac{f(DA_{\mathrm{SL}}, z) - f(DA_{\mathrm{PCA}}, z)}{f(DA_{\mathrm{SL}}, z)}$$
$$\simeq 1 - 1.12(1+z)^{-0.02}, \qquad (2)$$

$$CF_{\mathrm{IE2}}(z) = \frac{f(DA_{\mathrm{SL}}, z) - f(DA_{\mathrm{IE2}}, z)}{f(DA_{\mathrm{SL}}, z)}$$
$$\simeq 1 - 1.92(1+z)^{0.54}, \tag{3}$$

can be estimated using the power-law fits of $DA(z)$ given in Table 3.

These correction factors are shown in Fig. 5. To estimate the upper and lower limits of the correction factor, we used the errors of *DA* in Table 3. For the IE2 method, the error at a given z is taken as $\sqrt{\sigma_{\mathrm{IE2}}^2 + \sigma_{\mathrm{SL}}^2}$ where σ_{IE2} and σ_{SL} are the errors on the *DA* determination when we use the IE2 and SL methods. We fitted a smooth curve to these errors. Figure 5 gives at least an estimate of the mean error on *DA* induced by the use of the continuum fitting method.

7. Conclusion

In this paper, we have discussed four different continuum fitting methods: the power law (PL), principal component analysis (PCA), iterative estimate (IE), and smooth local (SL) methods to derive the continuum of quasars in the Lyman-α forest. The continuum is used in particular to determine the mean absorption of the IGM. The methods were applied to a sample of 20 high redshift highly luminous quasars ($m_{\mathrm{V}} \leq 17.5$ and $2.40 \leq z_{\mathrm{em}} \leq 3.91$) observed at intermediate resolution with either ESO-EMMI or OHP-CARELEC. Seven of these QSOs were also observed at high spectral resolution with VLT-UVES. We have measured the mean absorption in the IGM, *DA*, after estimating the continuum with the different methods applied to the same data. We derived its evolution with redshift by fitting a power law $DA(z) = A(1+z)^{\alpha}$ to measurements. The mean α index derived after combining results from different methods is ~ 2.1 (see Table 3). As can be seen in Fig. 2 and as expected, at low redshift, $z \sim 2$, there is not much difference between the *DA* values measured with different methods. But the results of the different methods disagree more and more as redshift increases. We then compare *DA* values measured along the same lines of sight but observed at very different spectral resolutions ($\sim$ 40,000 *versus* $\sim$ 2000). We find that *DA* estimates are similar in high and intermediate spectral resolution spectra, if we use the SL method. However, the SL method is not an automatic method and depends on subjective decisions. This problem can be overcome to a first approximation, if we make a correction factor, which should be applied to the results of an automatic method, the PCA or IE methods. These correction factors, of the order of 5–15% in the redshift range 2–3.5, are shown in Fig. 5. The correction factors we measure here are large enough that care should be exercised when applying one method or the other to the measurement of *DA*. We do think, however, that the best approach for this problem is probably to use a combination of these methods. This is something that should be investigated in the future.

Acknowledgements

AA was supported by a grant from the University of Sistan and Baluchestan and the Institute for Research in Fundamental Sciences (IPM) over the period of time used to complete this work.

Appendix – QSOs spectra and their different continua

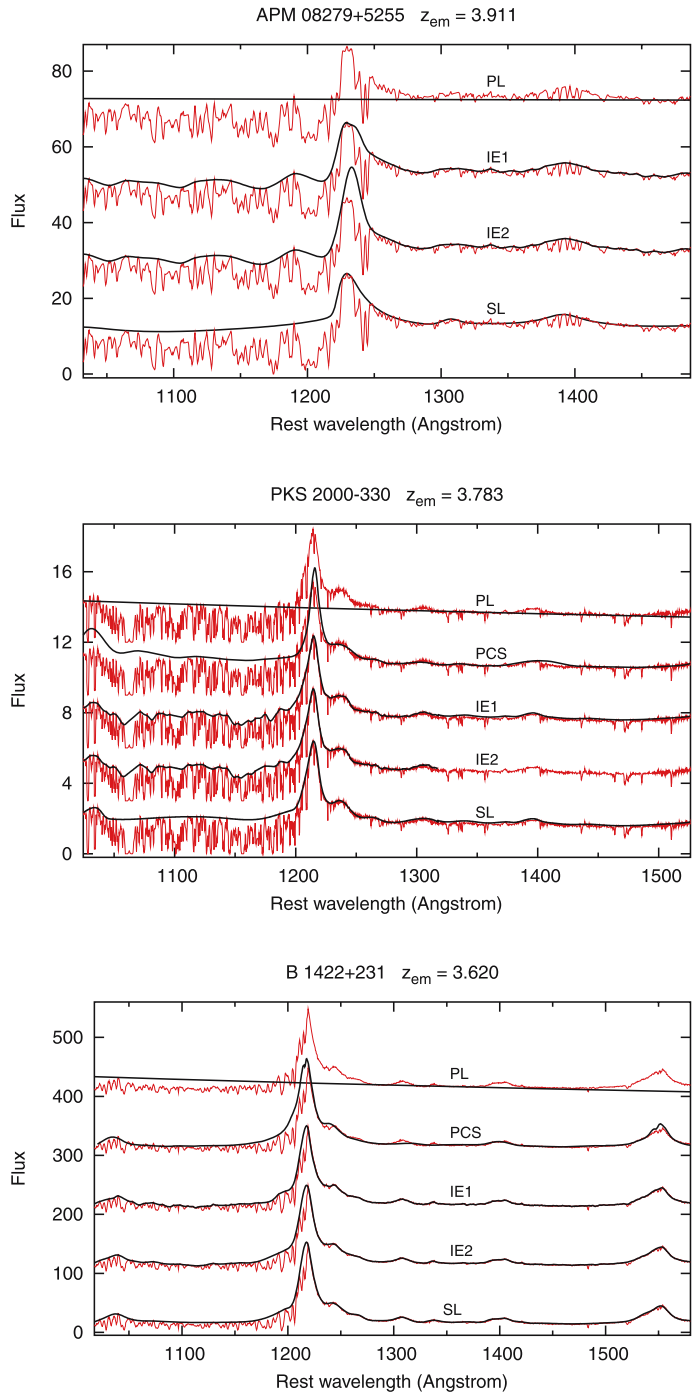

Figure A-1. QSO continua derived from applying the different methods described in section 4.

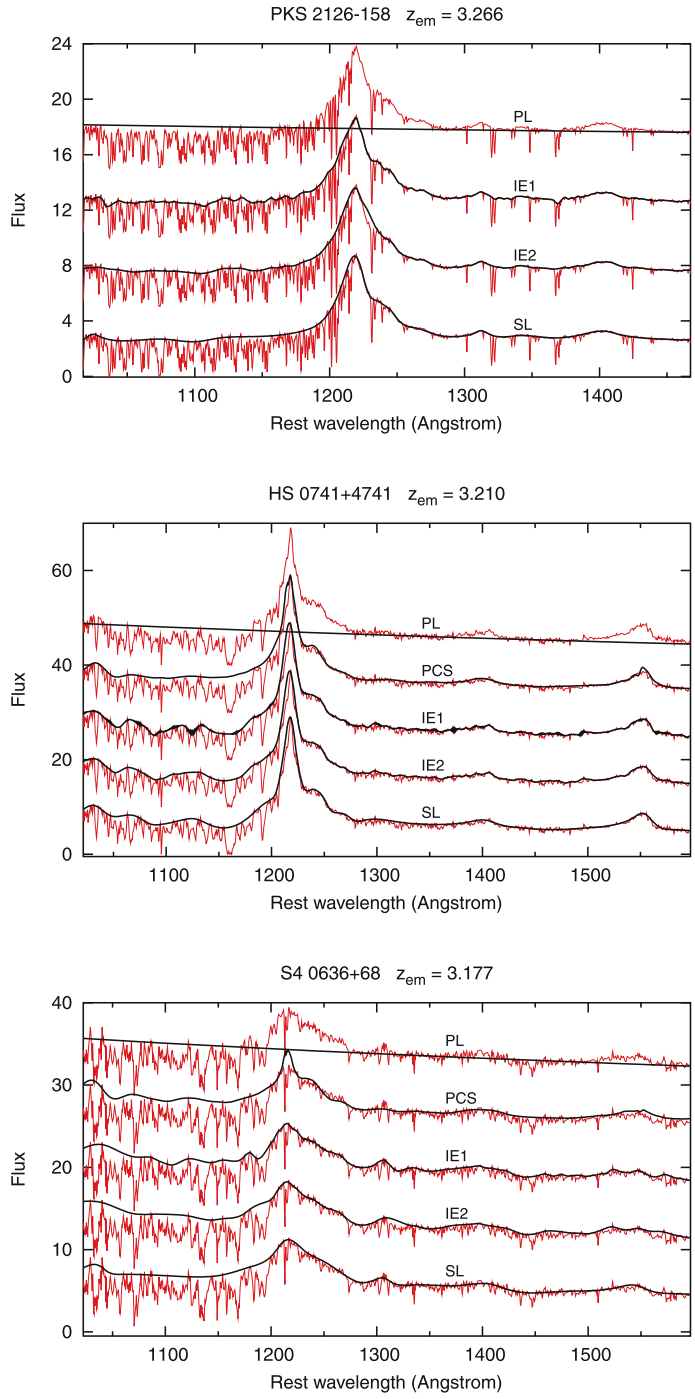

Figure A-1. (*Continued*).

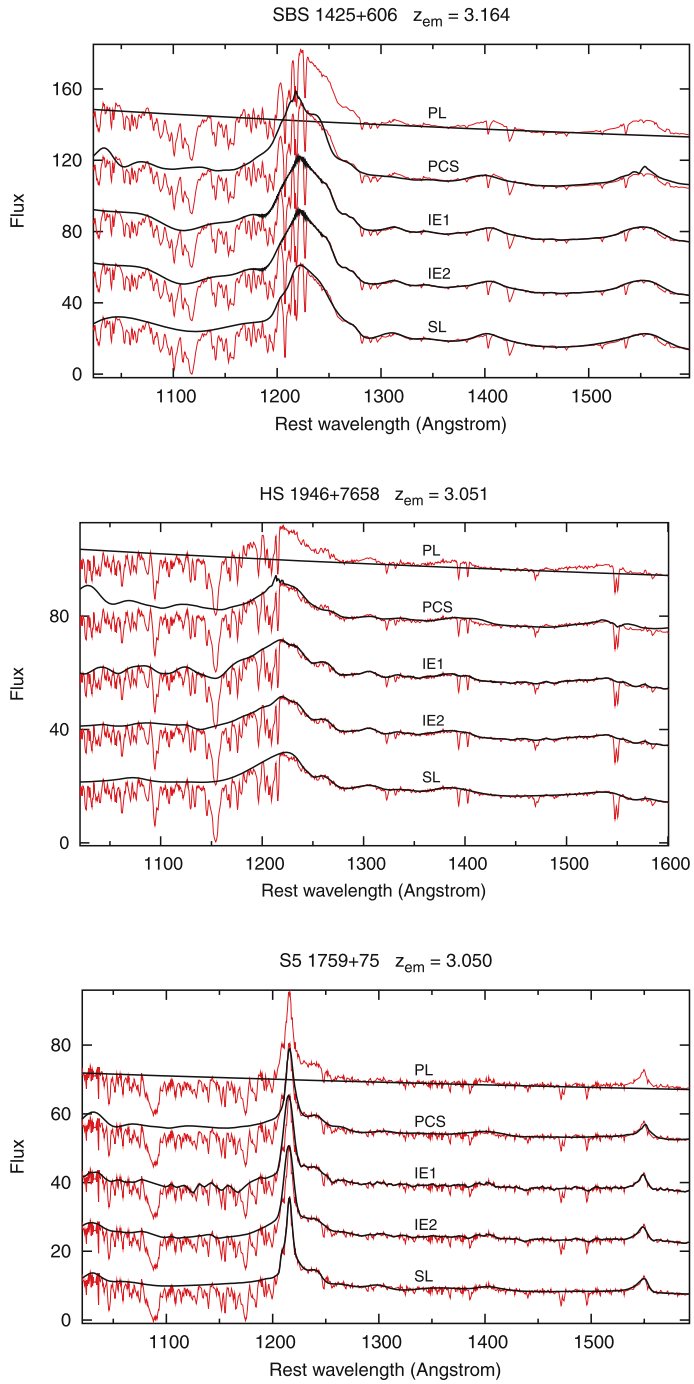

Figure A-1. (*Continued*).

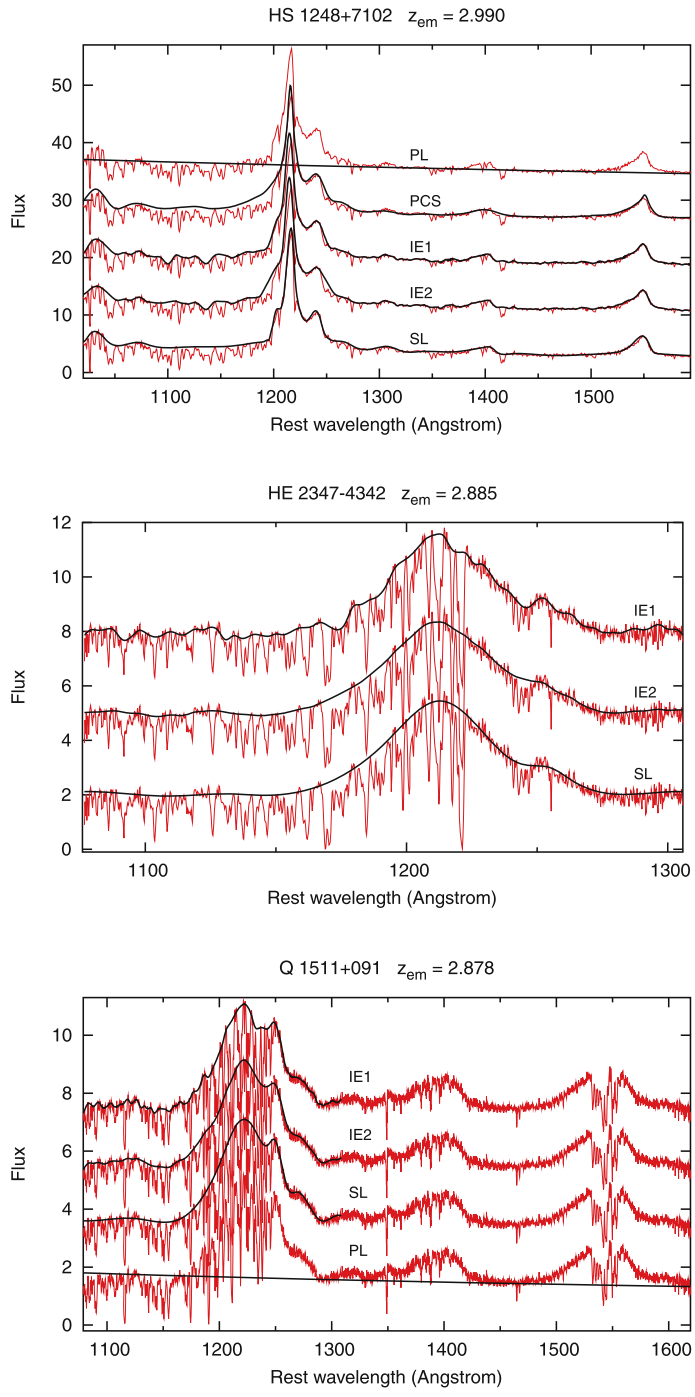

Figure A-1. (*Continued*).

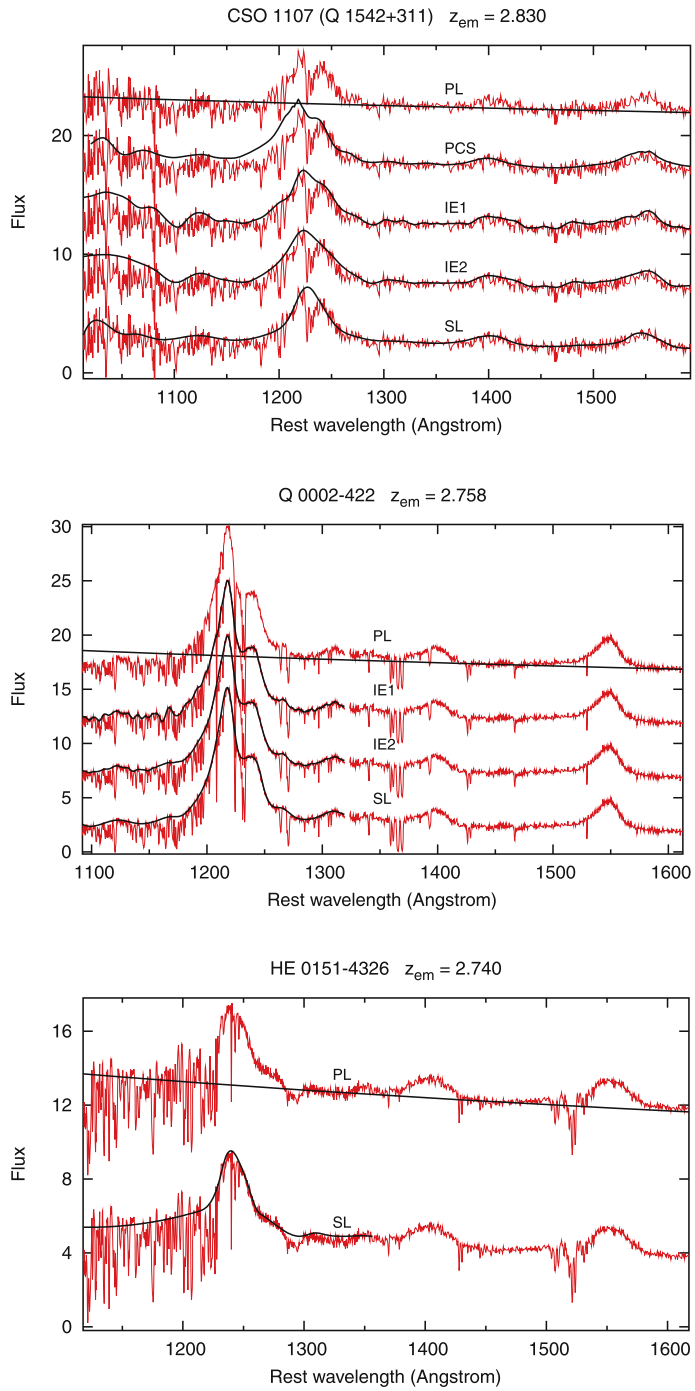

Figure A-1. (*Continued*).

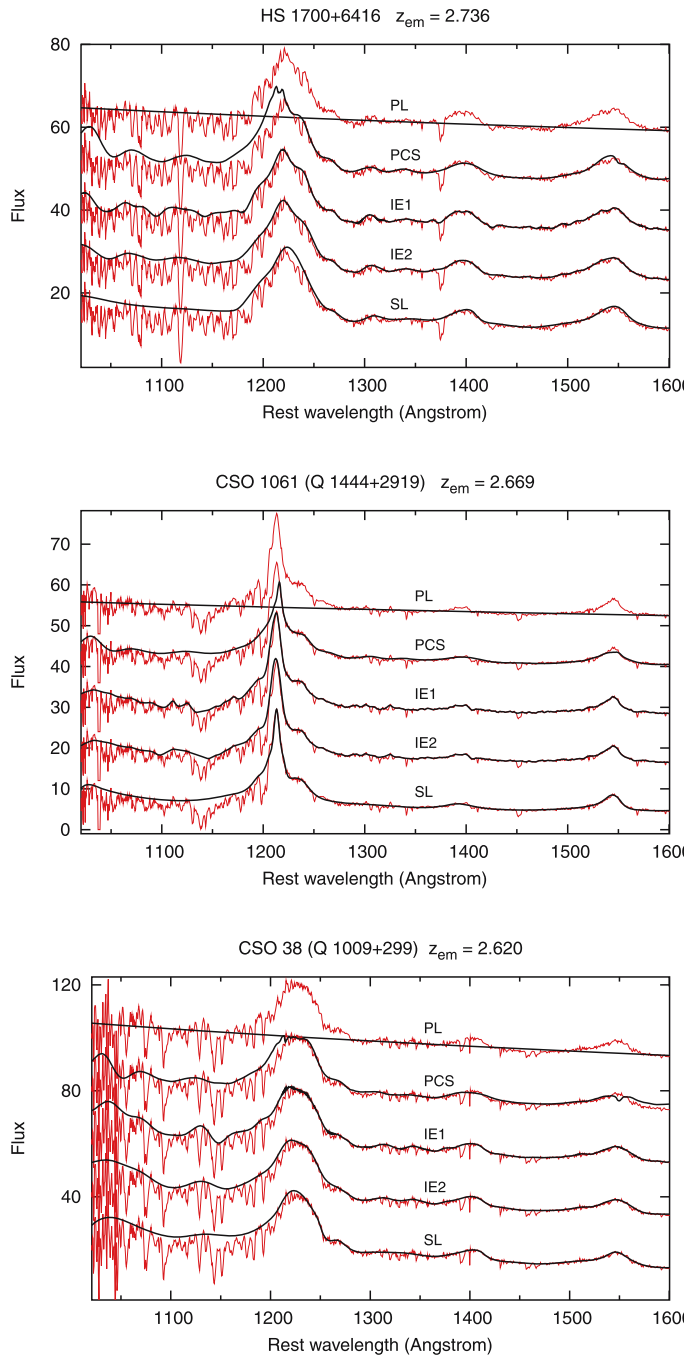

Figure A-1. (*Continued*).

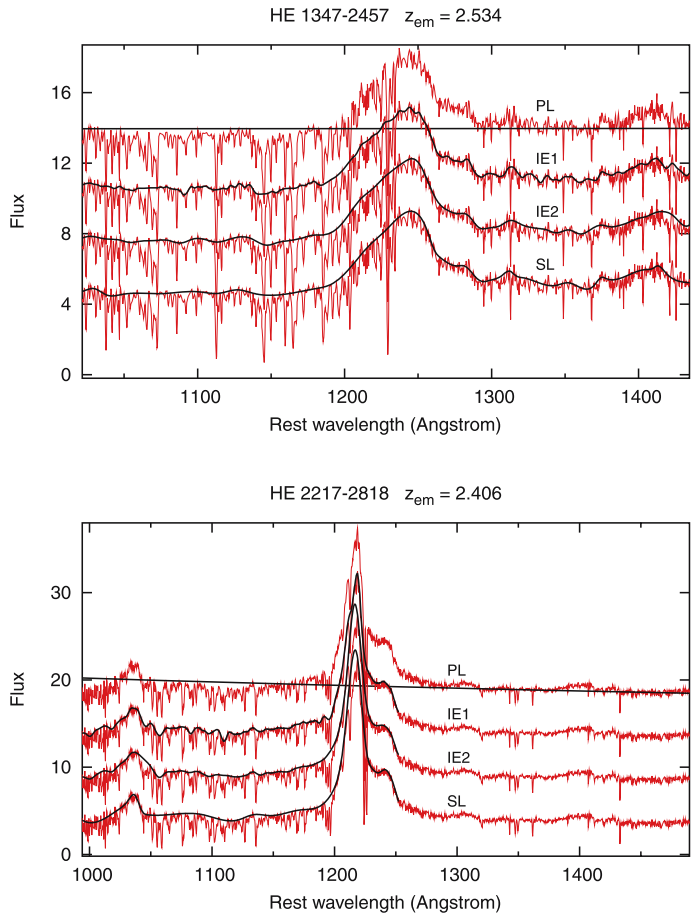

Figure A-1. (*Continued*).

References

Aghaee, A., Petitjean, P., Aracil, B., Coppolani, F., Theuns, T. 2005, In: *IAU Colloq. 199* (eds.) Williams, P. Shu, C.-G., Ménard, B., **199**, 397.
Aghaee, A., Petitjean, P., Aracil, B., Coppolani, F., Theuns, T. 2006, In: *PSI Colloq.*, 312.
Aracil, B., Petitjean, P., Pichon, C., Bergeron, J. 2004, *Astron. Astrophys.*, **419**, 811.
Becker, R. H. *et al.* 2001, *ApJ*, **122**, 2850.
Bernardi, M., Sheth, R. K., Subba Rao, M. *et al.* 2003, *Astron. J.*, **125**, 32.
Binette, L., Rodriguez-Martinez, M., Ballinas, I. 2003, *RMxAC*, **17**, 284.
Croft, R. A. C., Weinberg, D. H., Katz, N., Hernquist, L. 1998, *ApJ*, **495**, 44.
Croft, R. A. C., Weinberg, D. H., Pettini, M., Hernquist, L., Katz, N. 1999, *ApJ*, **520**, 1.
Dall'Aglio, A., Wisotzki, L., Worseck, G. 2009, *Submitted to the Astrophysical Journal*, astroph/0906.1484.
Edlén, B. 1966, *Metrologia*, **2**, 71.
Faucher-Giguère, C.-A., Lidz, A., Hernquist, L., Zaldarriaga, M. 2008, *ApJ*, **681**, 831.
Francis, P. J. 1996, *PASA*, **13**, 212.
Francis, P. J., Hewett, P. C., Foltz, C. B., Chaffee, F. H. 1992, *ApJ*, **398**, 476.
Gonzalez, J. F., Brillant, S., Hainaut, O. R., Sterzik, M. 2006, *The EMMI Manual*, **1**, 100p.
Gunn, J. E., Peterson, B. A. 1965, *ApJ*, **142**, 1633.
Horne, K. 1986, *PASP*, **98**, 609.

Kim, T.-S., Bolton, J. S., Viel, M., Haehnelt, M. G., Carswell, R. F. 2007, *MNRAS*, **382**, 1657.
Kim, T.-S., Cristiani, S., D'Odorico, S. 2001, *Astron. Astrophys.*, **373**, 757.
Kirkman, D., Tytler, D., Suzuki, N. *et al.* 2005, *MNRAS*, **360**, 1373.
Kirkman, D., Tytler, D., Lubin, D., Charlton, J. 2007, *MNRAS*, **376**, 1227.
McDonald, P., Seljak, U., Cen, R., Bode, P., Ostriker, J. P. 2005, *MNRAS*, **360**, 1417.
Nusser, A., Haehnelt, M. 2000, *MNRAS*, **313**, 364.
Pentericci, L., Rix, H.-W., Prada, F. *et al.* 2003, *Astron. Astrophys.*, **410**, 75.
Petitjean, P. 1999, *Annales de Physique*, **24**, 126p.
Pichon, C., Vergely, J. L., Rollinde, E., Colombi, S., Petitjean, P. 2001, *MNRAS*, **326**, 597.
Press, W. H., Rybicki, G. B., Schneider, D. P. 1993, *ApJ*, **414**, 64.
Rauch, M. 1998, *Ann. Rev. Astron. Astrophys.*, **36**, 267.
Rauch, M., Miralda-Escudé, J., Sargent, W. L. W. *et al.* 1997, *ApJ*, **489**, 7.
Richstone, D. O., Schmidt, M. 1980, *ApJ*, **235**, 361.
Sargent, W. L. W., Steidel, C. C., Boksenberg, A. 1989, *ApJS*, **69**, 703.
Schneider, D. P., Schmidt, M., Gunn, J. E. 1991, *ApJ*, **101**, 2004.
Seljak, U., McDonald, P., Makarov, A. 2003, *MNRAS*, **342**, L79.
Songaila, A. 2004, *AJ*, **127**, 2598.
Songaila, A., Cowie, L. L. 1996, *AJ*, **112**, 335.
Suzuki, N., Tytler, D., Kirkman, D., O'Meara, J. M., Lubin, D. 2005, *ApJ*, **618**, 592.
Theuns, T. 2005, In: *IAU Colloq. 199* (ed.) Williams, P., Shu, C.-G., Menard, B., p. 185.
Tytler, D., Kirkman, D., O'Meara, J. M. *et al.* 2004, *ApJ*, **617**, 1.
Vanden Berk, D. E. *et al.* 2001, *AJ*, **122**, 549.
Webster, R. L., Francis, P. J., Peterson, B. A., Drinkwater, M. J., Masci, F. J. 1995, *Nature*, **375**, 469.
White, R. L., Becker, R. H., Fan, X., Strauss, M. A. 2003, *Astron. J.*, **126**, 1.
Zheng, W., Kriss, G. A., Telfer, R. C., Grimes, J. P., Davidsen, A. F. 1997, *ApJ*, **475**, 469.